Supplementary Information for the paper

Low-symmetry vacancy-related spin qubit in hexagonal boron nitride

Rohit Babar[1,2,†], Gergely Barcza[1,2,†], Anton Pershin[1,3,†], Hyoju Park[4], Oscar Bulancea Lindvall[5], Gergő Thiering[1], Örs Legeza[1,6], Jamie H. Warner,[4] Igor A. Abrikosov[5], Adam Gali[1,3,*], and Viktor Ivády[2,5,8,*]

[1]*HUN-REN Wigner Research Centre for Physics, PO Box 49, H-1525, Budapest, Hungary*

[2]*MTA–ELTE Lendület "Momentum" NewQubit Research Group, Pázmány Péter, Sétány 1/A, 1117 Budapest, Hungary*

[3]*Department of Atomic Physics, Insitute of Physics, Budapest University of Technology and Economics, Műegyetem rakpart 3., H-1111, Budapest, Hungary*

[4]*Walker Department of Mechanical Engineering and Materials Graduate Program, Texas Materials Institute, The University of Texas at Austin, Austin, Texas 78712, United States*

[5]*Department of Physics, Chemistry and Biology, Linköping University, SE-581 83 Linköping, Sweden*

[6]*Institute for Advanced Study, Technical University of Munich, Lichtenbergstrasse 2a, 85748 Garching, Germany*

[7]*MTA-WFK Lendület "Momentum" Semiconductor Nanostructures Research Group, PO Box 49, H-1525, Budapest, Hungary*

[8]*Department of Physics of Complex Systems, Eötvös Loránd University, Egyetem tér 1-3, H-1053 Budapest, Hungary.*

†*Contributed equally.*

**email:gali.adam@wigner.hu; ivady.viktor@ttk.elte.hu*

July 2, 2024

Contents

1 Supplementary Note 1 - Discussion on the methodology

In this study, we utilize three state-of-the-art first-principles computational methods to provide a reliable and highly accurate description of the electronic structure of the VB2 defect. Our workhorse is the self-consistent hybrid density functional theory (DFT) with a modified HSE06[1,2] exchange-correlation function using 0.32 mixing parameter[3]. Hereinafter, we refer to this method as HSE(0.32). HSE(0.32) provides convergent and accurate values for all the considered ground state properties as well as for excited state energies and geometries when the excited state wavefunction can be approximated by a single Slater determinant. It is not guaranteed in general that the last requirement is fulfilled for all the excited states, thus higher-level wavefunction-based methods are needed to support the DFT calculations. Here we note that the most relevant low-energy excited states of the VB2 defect are found to be single Slater determinant, thus we can use the HSE(0.32) method to study them as well.

Second, we use n-electron valence state perturbation theory (NEVPT) to study the excited state spectrum. This method first describes the defect state on CASSCF level of theory and then, accounts for the dynamic correlation with the orbital outside the active space by the second-order perturbation theory. The method yields a convergent and quantitatively accurate spectrum even for the higher-lying excited states. Due to the computational complexity, we use an 8 orbital 8 electron active space to describe the most relevant electronic transitions among the defect states. A clear advantage of this approach is that, besides the excitation energies, the transition properties between the correlated wavefunctions (CASSCF) are readily available in the applied computational code.

Lastly, we use the density matrix renormalization group (DMRG) method to study the excited state spectrum. This wave function method is particularly suitable to describe strongly correlated effects, where the corresponding Hamiltonian is constructed according to the complete active space protocol. In order to minimize the uncertainties due to the active space selection, we studied active space composed of 100 orbitals. We expect that all the relevant multiplets are found in our DMRG calculations. Comparison of the DMRG, NEVPT, and HSE(0.32) results helps us to define the most relevant orbitals and to obtain reliable and convergent results. For the low energy part of the spectrum, we obtain remarkable agreement between all the methods.

2 Supplementary Note 2 - Fabrication

* Details on the formation energy calculations

In a layered host material like hBN, vacancy complexes may be formed by vacancies in the same layer (in-plane complexes) as well as by vacancies in different adjacent layers (inter-plane complexes).[4] According to recent theoretical studies the binding energy of the latter is only 0.4 eV in the most favorable configuration.[4] Note that, annealing at moderate temperature could unbind such an inter-layer complex. An adjacent pair of in-plane boron vacancies results in a highly unstable configuration where the nitrogen atom between the two vacancies possesses two dangling bonds and binds only to a single boron atom, see Fig. 1a of the main text. This unstable configuration transforms into an energetically favorable isostoichiometric configuration that consists of an adjacent boron vacancy, a nitrogen vacancy, and a nitrogen anti-site ($V_BV_NN_B$), see Fig. 1b and 1d of the main text, which is referred as VB2 configuration hereinafter. Due to the appearance of strong nitrogen-nitrogen bonds, the formation of the VB2 complex is highly favorable. Indeed, we obtain 5.14 eV binding energy for a pair of neutral boron vacancy in the relaxed structure on HSE(0.32) level of theory, in good agreement with a previous work[4].

The formation energy curves of the VB2 and the V_B defects as a function of the Fermi energy are depicted in Fig. 1c of the main text. As one can see, V_B possesses three stable charge states in the band gap with charge transition levels at 1.96 eV and 4.60 eV. Note that these charge transition levels are similar but deviate by +0.48 eV and -0.3 eV from previous calculations[3]. We attribute these differences to the distinct computational details. We utilized a large supercell of 768 atoms in contrast to the 240-atom supercell used in the prior work[3]. Depending on the position of the Fermi level, the VB2 defect exhibits four stable charge states and three charge transition levels, $(+1/0)$, $(0/–1)$, and $(-1/–2)$ at 1.78 eV, 3.61 eV, and 4.90 eV in the band gap of hBN, see Fig. 1c of the main text. Due to the large binding energy of the VB2 configuration, the formation energy of the mono-vacancy and the VB2 complex are comparable, especially in boron-poor conditions. For Fermi energies approaching the valence band maximum, the formation energy of the positively charged VB2 complex is below 10 eV, and approaching the formation energy of the neutral boron vacancy. This opens a possibility for a direct creation of VB2 defects in a high-temperature thermal

equilibrium growth process with p-type doping.

*** Fabrication in few layer hBN**

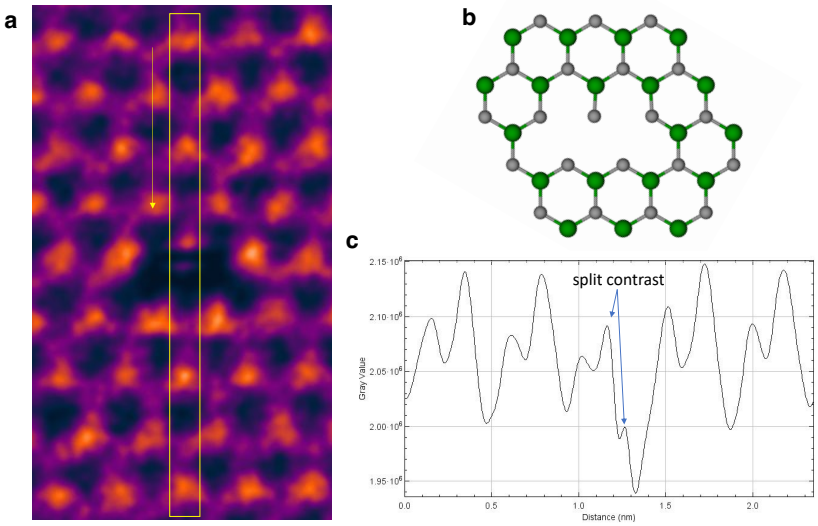

Supplemental Figure 1: **a** STEM image of the metastable boron divacancy configuration. **b** Structure of the boron divacancy configuration for comparison. **c** Intensity profile along the yellow box in **a**.

As we have discussed in the main text, the VB2 defect is readily observed in our STEM measurements in a single-layer hBN sample. In addition to the relaxed VB2 configuration, we also observe the metastable configuration of boron double vacancies in our STEM images, see Supplementary Figure 1a and b. As this defect configuration is short-lived, we anticipate that the divacancy defect is created by the electron beam of the STEM microscope when scanning through a single boron vacancy defect in the hBN sample. Indeed, the electron beam dominantly displaces boron atoms and creates boron vacancy-related defects. Furthermore, atoms close to defective sites are removed more frequently, thus the electron beam tends to create larger defect clusters.

The nitrogen atom between the two boron vacancies is unstable. As can be seen in Supplementary Figure 1c, the contrast of this atom is weak and split expectedly due to its movement. The unstable nitrogen atom may either relax into one of the vacancy sites and form the VB2 configuration or leave the defect due to the out-of-plane momentum received from the electron beam and

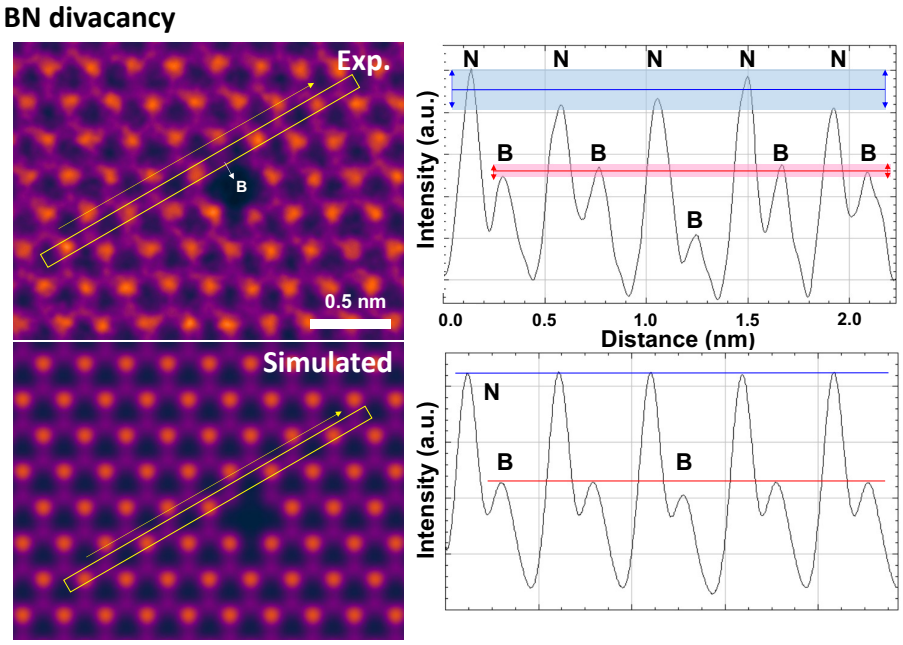

Supplemental Figure 2: STEM image and intensity profile of the boron-nitrogen divacancy configuration in hBN. The left top and left bottom panels show the experimental STEM image and corresponding simulation. The right panels depict the intensity profile along the yellow box.

give rise to a tri-vacancy configuration.

Supplementary Figure 2 shows the STEM image of the boron-nitrogen divacancy in hBN. Note that the boron atom at the edge has a darker contrast due to the low density of electrons. Compared to Fig. 1 of the main text, the differences between the STEM images of the VB2 and divacancy configurations are apparent.

These results show that the VB2 configuration may be intentionally created by a focused electron beam in a well-defined location. This fabrication mechanism may hold not only for a single layer but also for few-layer samples. The latter configuration is more favorable in applications when the defect states need to be protected from environmental contaminants adsorbed on the surface of the sample.

*** Fabrication in bulk**

Single boron vacancies are routinely created nowadays by after-growth processing, in particular, by irradiation[5–7], ion implantation[6,8,9], and laser writing[10]. As the VB2 configuration is isostoichiometric to a boron vacancy pair, migration of boron vacancy may naturally form the VB2 configuration. Once the boron vacancies get close enough to each other, the 5.14 eV energy release upon the formation of the VB2 configuration ensures the stability of the complex. To optimize such a boron vacancy migration-driven fabrication process, high irradiation doses may be desirable to ensure that the boron vacancy is the dominant defect and simultaneously pins the Fermi level within the band gap. When neutral boron vacancies are present in the sample, their aggregation is not hindered by the Coulombic repulsion. The high vacancy concentration may also be advantageous for the formation of vacancy complexes.

According to recent theoretical studies[3], interstitial boron and nitrogen atoms are mobile even at room temperature, while the neutral boron and nitrogen vacancies are mobilized only at 1000 K and 1800 K, respectively. Therefore, annealing a highly irradiated hBN sample at 1000 K may lead to the formation of the VB2 configuration. We note, however, that the creation of larger vacancy complexes may also take place, thus the annealing temperature and time should be optimized.

3 Supplementary Note 3 - Electronic structure

* Single particle electronic structure

The single particle energy levels of the neutral VB2 defect as obtained from HSE(0.32) calculations are depicted in Supplementary Figure 3a. As can be seen, there are multiple occupied and unoccupied states appearing either inside or close to the band gap of hBN. To understand the electronic structure of the defect, we consider the four sp^2 dangling bonds and the four p_z orbitals of the three nitrogen atoms and the boron atom neighboring the double vacancy site ($V_B V_N$) of VB2. The eight defect states are occupied by 10 electrons in the neutral charge state. Note that due to the nitrogen-nitrogen bonds of the VB2 defect, other localized states are also formed that lie in the valence band and mix slightly with other orbitals. For simplicity, we ignore them in the discussion of the electronic structure and focus only on the dangling bonds and p_z orbitals of the four first nearest neighbor atoms.

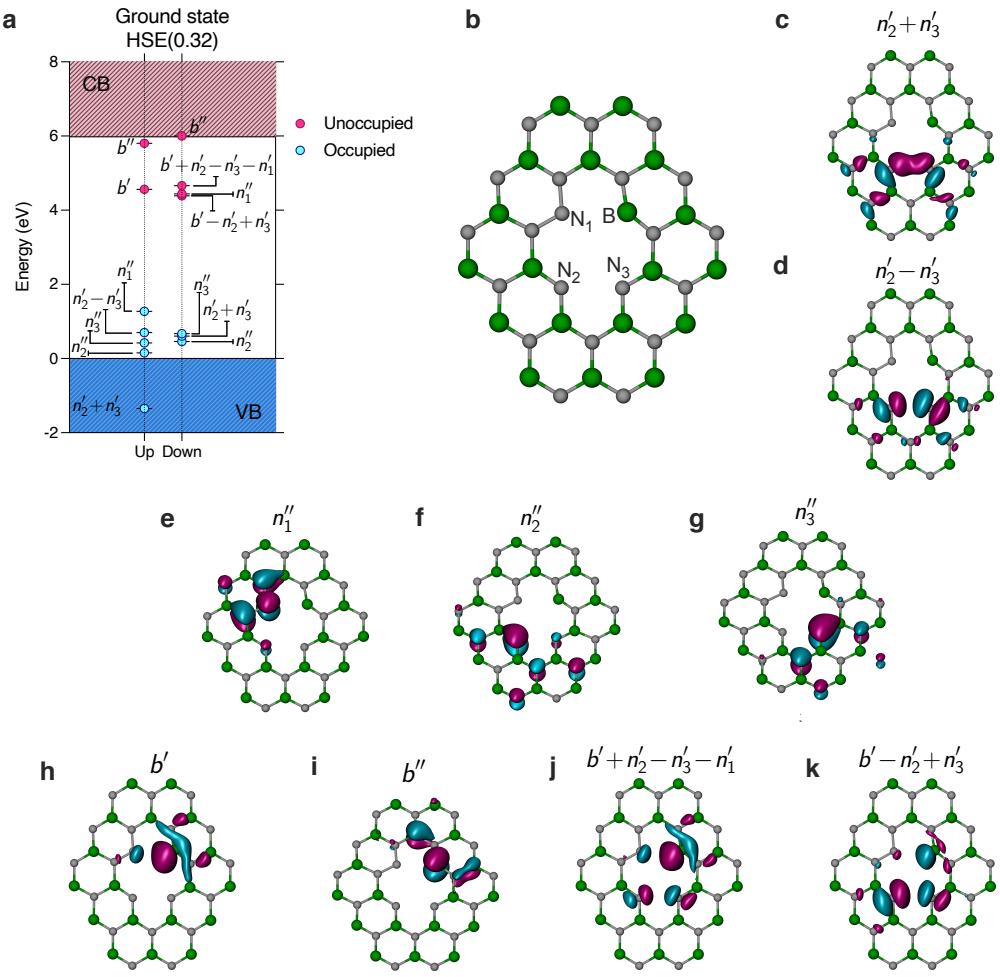

Supplemental Figure 3: Electronic structure and localized Kohn-Sham orbitals of the VB2 defect. **a** Single particle electronic structure of the triplet ground state as obtained by HSE(0.32) functional. Lines with colored points represent the most relevant defect states inside and close to the band gap of hBN. **b** Structure of VB2 with labels of the first neighbor atoms of the divacancy site. **c**-**k** Wavefunctions of defect states labelled in **a**.

The highest possible point group symmetry of the stable VB2 configuration is C_{1h} that contains only a single in-plane reflection operator beside the identity operator and possesses two one-dimensional irreducible representations, A′ and A″. Considering s and p atomic orbitals of the host material, only the p_z orbital transforms according to A'' in our coordinate system where the z axis

is parallel to the c-axis.

Due to the low symmetry and complexity of the defect, irreducible representations alone are not sufficient to unambiguously label the defect states. Therefore, we use the lowercase labels of the first neighbor atoms, n_1, n_2, n_3, and b, see Supplementary Figure 3b, on which the states are dominantly localized, and prime and double prime superscripts of the irreducible representation of the states. For example, n_1'' refers to an orbital that dominantly localized on atom N_1 and transforms according to A'' irreducible representation. When an orbital is localized on more than one first neighbor atoms, linear combinations of the site-dependent notations label the orbitals, e.g. $n_2' \pm n_3'$ refers to an in-plane bonding and anti-bonding states between nitrogen N_1 and N_2, respectively. This combined notation enables us to unambiguously label the most relevant states in and close to the band gap.

Each of the defect energy levels depicted in Supplementary Figure 3a is labeled after analyzing the corresponding single-particle wavefunctions, depicted in Supplementary Figure 3c-k. The three states localized on the first neighbour nitrogen atoms with out-of-plane symmetry, i.e. n_1'', n_2'', and n_3'', are all found in the band gap in both spin channels. In the spin-up channel, they are all occupied and nearly degenerate, while in the spin-down channel only n_2'' and n_3'' are occupied and located close to the valence band edge with similar energy. Besides these states we find partially occupied bonding and anti-bonding combinations of the in-plane dangling bonds localized on N_2 and N_3 atoms, i.e. $n_2' \pm n_3'$. In the spin-up channel, both the bonding and the anti-bonding states are occupied with the latter being higher in energy, while in the spin-down channel, only the bonding state is occupied. The unoccupied states in the spin-up channel are formed by the in-plane and perpendicular-to-plane symmetric states of the first neighbor boron atom. In the spin-down channel, two additional unoccupied states appear, n_1'' and the anti-bonding $n_2' - n_3'$ that heavily mix with the b' state.

As the defect orbitals of the VB2 center have the tendency to form nearly degenerate states in the band gap close to the valence band edge, a high-spin ground state may be formed. From the electronic structure and the single particle wavefunctions depicted in Supplementary Figure 3, one can identify that the n_1'' and the $n_2' - n_3'$ states are half occupied. Indeed, these orbitals account

dominantly for the spin density depicted in Fig. 3a of the main text.

* Singlet-triplet gap in the GS manifold

The two half-filled states, giving rise to the high-spin ground state, have different characters and are localized on different atoms. This feature has an important effect on the electronic structure. As the exchange energy between the two states is marginal and the singlet-triplet wavefunctions are nearly identical, the singlet-triplet gap is unprecedentedly small compared to existing point defect qubits. By carrying out open-shell singlet calculations with PBE and HSE(0.32) functionals, we find that the triplet ground state is favorable by only 4.3 meV and 3.3 meV, respectively. To further confirm our DFT results, we carry out NEVPT2 and multireference DMRG calculations on HSE(0.32) relaxed ground state VB2 configuration in a single sheet hBN model and obtain 10 meV and 12 meV singlet triplet vertical gap. Here, we note that the closed-shell singlet state is highly unfavorable, i.e. it is 1.3 eV higher in energy than the triplet ground state on HSE(0.32) level of theory.

4 Supplementary Note 4 - Excited states and decay processes

* Excited states

Due to the numerous defect energy levels found in the band gap of hBN, one may expect several excited states below the ionization threshold with diverse decay routes that may result in photoluminescence as well as spin-selective non-radiate decay through inter-system crossings (ICSs) between the triplet and singlet manifolds. Such processes are indispensable for an applicable qubit, as they make optical spin initialization and readout possible.

The HSE(0.32), NEVPT2, and DMRG vertical spectra as obtained on the ground state atomic configurations are provided in Supplemental Table 1. For a recent study on the excitation properties of VB2 see also Ref. [11]. Note that the labeling of the states is defined based on their zero-phonon photoluminescence transition energies, therefore, the states in the vertical, absorption energy spectrum do not appear in order. All computational approaches consistently predict nearly degenerate pairs of singlet and triplet states throughout the spectrum. In particular, besides the singlet-triplet

Supplemental Table 1: Vertical energy spectra on the HSE(0.32) ground state atomic configuration as obtained with our methods. Labeling of the many-body states follows the labeling introduced in Fig. 2a of the main text. All values are in eV.

state	transition	HSE(0.32)	NEVPT2	DMRG
T0@GS	GS	0.000	0.000	0.000
S0@GS	–	0.003	0.010	0.012
S2@GS	$n_2'' \rightarrow n_2' - n_3'$	1.855	1.993	1.603
T2@GS	$n_2'' \rightarrow n_2' - n_3'$	1.970	2.140	1.672
T1@GS	$n_1'' \rightarrow b'$	2.343	2.279	4.243
S1@GS	$n_1'' \rightarrow b'$	2.362	2.277	4.283
S3@GS	$n_3'' \rightarrow n_2' - n_3'$	2.4154		3.072
T3@GS	$n_3'' \rightarrow n_2' - n_3'$	2.417	2.541	3.070
T4@GS	$n_2' + n_3' \rightarrow n_2' - n_3'$			3.601
S4@GS	$n_2' + n_3' \rightarrow n_2' - n_3'$			3.620

pair in the ground state, we observe four additional pairs with excited state energies below the ionization threshold for the ground state configuration. We note that the excited state wavefunction obtained by NEVPT2 and DMRG methods can be well-characterized by a single Slater determinant. This observation enables us to use a less-demanding self-consistent field theory, such as the constrained occupation DFT method[12], to study the excited state properties and carry out structural relaxation. Furthermore, as the ground state and all the excited states are dominantly single determinants, the latter can be characterized by a single electronic transition between the occupied and unoccupied orbitals of the ground state, see Supplemental Table 1.

As can be seen in Supplemental Table 1, we achieve remarkable quantitative agreement between the HSE(0.32) and NEVPT energy spectra that further support the use of the HSE(0.32) method for studying the VB2 center. The DMRG results agree well with the other method in the energy of the first optically excited triplet T2 and singlet S2 states. The energy of the T1 and S1 excited states is overestimated in DMRG compared to the NEVPT values. We attribute this difference to the lack of a sufficiently large number of unoccupied orbitals in the active space. The inclusion of higher-lying virtual states is expected to improve the description of the b' and b'' related multiplets. Note that the DMRG calculation finds other high-energy excited states, T4 and S4. As we will see later, this high-energy state does not play a role in the low-energy excitation processes.

The reason behind the appearance of singlet-triplet pairs throughout the spectrum is similar to what we have earlier seen for the S0 excited and the T0 ground states, i.e. the half-filled defect orbitals are localized on opposite sides of the defect that results in unusually small exchange energy in the triplet state. The observed excited triplets exhibit a similar feature, as the dominant transitions involve only such orbitals that localized either on the N_2 and N_3 atoms or on the N_1 and B atoms, see Supplemental Table 1. Therefore, the separation and overlap of the unpaired electrons are unaffected by these excitation processes. Note also that the relaxed geometries of the triplet and singlet states are nearly identical. Therefore, hereinafter we calculate the energy spectrum only on the triplet excited state geometries.

In order to analyze possible decay pathways, we calculate the vertical energy spectrum ob-

Supplemental Table 2: Vertical energy spectra as obtained on different HSE(0.32) relaxed excited state geometries. The energy of the ground state electronic configuration on the excited state configurations is set as the zero value of the energy scale. All values are in eV.

configuration	state	transition	HSE(0.32)	NEVPT2	DMRG
T1	T1	$n_1'' \rightarrow b'$	-0.225		-0.155
	S1	$n_1'' \rightarrow b'$			-0.095
	T0	GS	0.000	0.000	0.000
	S0	–			0.004
	Tm	$n_3'', n_1'' \rightarrow n_2' - n_3', b'$			1.269
	Sm	$n_3'', n_1'' \rightarrow n_2' - n_3', b'$			1.295
	Tn	$n_3'', n_2'' \rightarrow n_2' - n_3'$			1.818
	Sn	$n_3'', n_2'' \rightarrow n_2' - n_3'$			1.862
T2	T0	GS	0.000	0.000	0.000
	S0	–		0.011	0.015
	T2	$n_2'' \rightarrow n_2' - n_3'$	1.248	1.321	0.900
	S2	$n_2'' \rightarrow n_2' - n_3'$	1.330	1.206	0.858
	S3	$n_3'' \rightarrow n_2' - n_3'$		2.239	3.752
	T3	$n_3'' \rightarrow n_2' - n_3'$		2.248	3.748
	T4	$n_2' + n_3' \rightarrow n_2' - n_3'$			3.880
	S4	$n_2' + n_3' \rightarrow n_2' - n_3'$			3.906
	S1	$n_1'' \rightarrow b'$		3.648	4.514
	T1	$n_1'' \rightarrow b'$		3.653	4.230
T3	T0	GS	0.000	0.000	0.000
	S0	–	-0.002	0.003	0.005
	S3	$n_3'' \rightarrow n_2' - n_3'$	1.423	1.840	1.297
	T3	$n_3'' \rightarrow n_2' - n_3'$	1.428	1.840	1.291
	S2	$n_2'' \rightarrow n_2' - n_3'$		2.119	2.081
	T2	$n_2'' \rightarrow n_2' - n_3'$		2.349	2.267
	T4	$n_2' + n_3' \rightarrow n_2' - n_3'$			2.679
	S4	$n_2' + n_3' \rightarrow n_2' - n_3'$			2.712
	T1	$n_1'' \rightarrow b'$		3.814	3.423
	S1	$n_1'' \rightarrow b'$		3.826	3.529

Supplemental Table 3: Mean absolute error (MAE) and mean absolute percentage error (MAPE) of the first optically excited state energies obtained on four different atomic configurations (GS, T1, T2, and T3) with different computational methods.

methods	MAE (eV)	MAPE (%)
HSE(0.32)-NEVPT	0.222	13.6
HSE(0.32)-DMRG	0.234	23.2
NEVPT-DMRG	0.453	31.2

tained on HSE(0.32) relaxed geometries of the T1, T2, and T3 excited states in Supplemental Table 2. As can be seen for the T1 and T2 configurations, the first optical excited state is always the corresponding excited state, i.e. on the T2(T3) HSE(0.32) geometry the T2(T3) and S2(S3) excited states are the lowest energy optically excited states. Furthermore, the first excited energy gaps are smaller than the absorption energies provided in Supplemental Table 1. This indicates that the HSE(0.32) properly captures the nature of the many-body excited states.

The case of the T1 configuration needs further discussion. In the HSE(0.32) calculations we observe a significant structural relaxation for the $n_1'' \rightarrow b'$ transition that affects both T1 and S1 excited states. Due to the 1.34 eV relaxation energy of the T1 excited state and the 1.2 eV increase of the energy of the ground state electronic configuration, the T1 and the ground state swap so that T1 becomes the ground state on the corresponding atomic configuration and the ground state occupation appears as the first excited state. Importantly, this huge relaxation effect is confirmed by the DMRG calculations where the two states are also swapped. We note that the higher-lying excited states on the T1 geometry have a multi-determinant character in contrast to the trend seen for other geometries. In the NEVPT calculations on the T1 configuration, we cannot find a suitable active space to accurately describe the spectrum.

While Supplemental Table 1 and Supplemental Table 2 provide the full spectrum on all the geometries, the most relevant values for the current study are the first excited state energies. The mean absolute error (MAE) and the mean absolute percentage error (MAPE) of different methods

for the first optically excited state energy are provided in Supplemental Table 3. As can be seen, a low margin of error is achieved for the lowest energy excited states despite the different models and computational methods used. Since for single Slater determinant excited states the self-consistent HSE(0.32) method provides the most convergent and most accurate results, hereinafter we use this method if not stated otherwise.

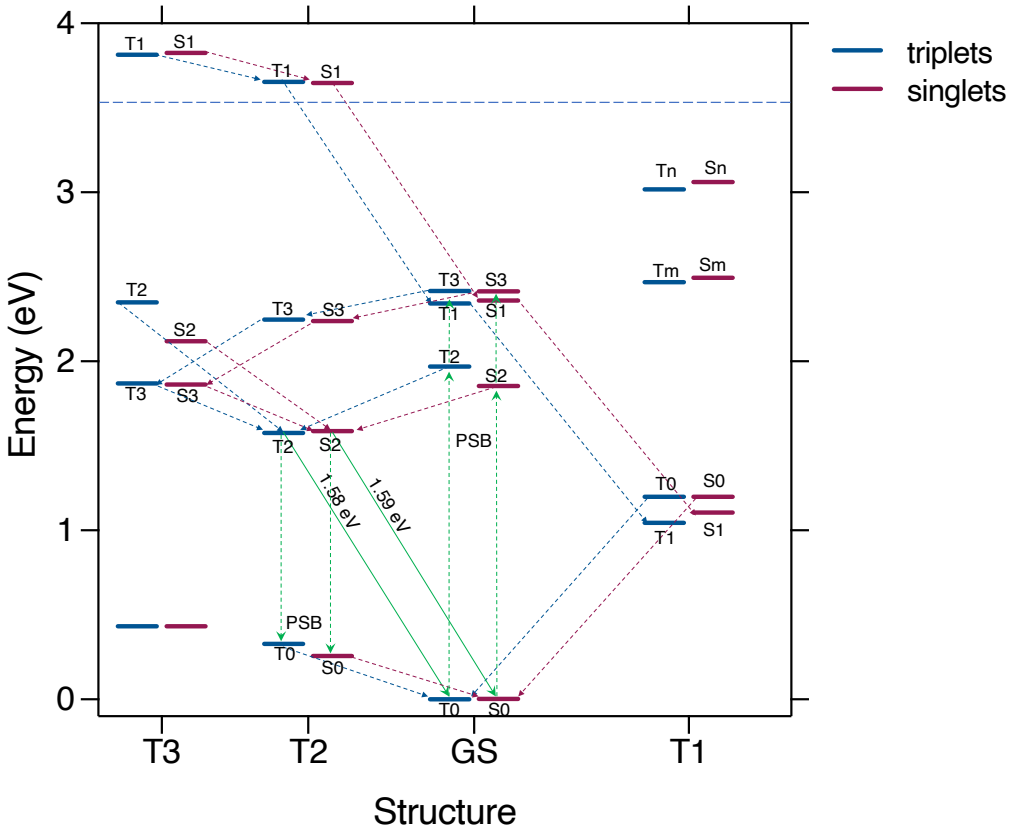

Supplemental Figure 4: Energy level structure as obtained on the HSE(0.32) relaxed ground state (GS), first excited triplet state (T1), second excited triplet state (T2), and the third excited triplet state (T3) geometries. Red and blue dashed arrows indicate non-radiative spin-conserving transitions, i.e. structural relaxation through the emission of phonons, green solid arrows indicate ZPL optical transitions and green dashed arrows indicate phonon-assisted optical transitions, giving rise to phonon side bands (PSB). The blue dashed horizontal line indicates the ionization threshold.

The electronic structure is summarized in Supplementary Figure 4 which shows the four

Supplemental Table 4: ZPL energies, radiative decay rates (r_{rad}), and quantum efficiency (QE) as obtained by the HSE(0.32) method. For more details on the non-radiative decay and quantum efficiency see Supplemental Table 5 and the text.

configuration	transition	ZPL (eV)	r_{rad} (MHz)	QE
T1	$n_1'' \rightarrow b'$	0.975	–	0
S1	$n_1'' \rightarrow b'$	0.950	–	0
T2	$n_2'' \rightarrow n_2' - n_3'$	1.578	3.18	0.148
S2	$n_2'' \rightarrow n_2' - n_3'$	1.586	2.57	0.123
T3	$n_3'' \rightarrow n_2' - n_3'$	1.869	1.15	3.85×10^{-5}
S3	$n_3'' \rightarrow n_2' - n_3'$	1.863	1.61	5.40×10^{-5}

considered atomic configurations and the corresponding vertical energy spectra. Dashed blue and red lines indicate the structural relaxation of the different excited states to visualize the variation of the energy spectrum on different atomic configurations.

The calculated ZPL energies for the six lowest energy triplet and singlet excited states are provided in Supplemental Table 4. The expected error bar for the calculated values is ≈0.1 eV.

*** Spin-conserving decay and optical signal**

At first, we examine spin-conserving non-radiative decay pathways from the lowest three excited states in the triplet manifold. Note that our discussion is also valid for the singlet manifold due to the observed pairing of the singlet-triplet states. The configuration coordinate diagrams for the lowest two triplet excited states, T1 and T2, and the for the ground state are depicted in Supplementary Figure 5. As can be seen, the lowest energy excited state T1 goes through a huge structural relaxation after absorbing a photon in the ground state configuration. At the same time, the ground state configuration becomes highly unfavorable on the relaxed T1 structure, thus the T1 excited state appears to be lower in energy. According to the Seitz model, no photoluminescence is expected from the T1 excited states in this case, see Supplemental Table 4. Therefore, excitation

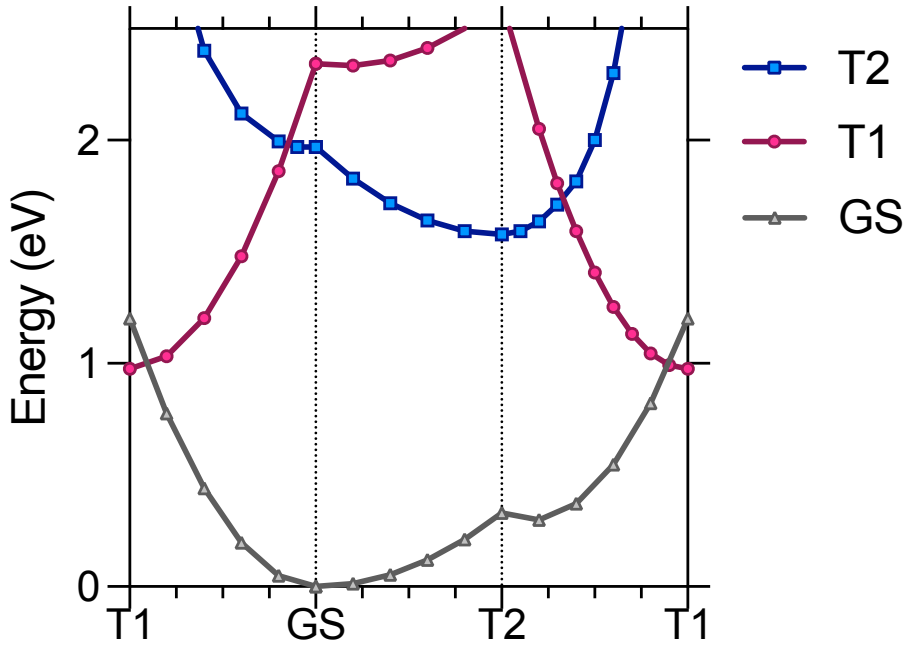

Supplemental Figure 5: Configuration coordinate diagram for T1 and T2 excited states and the ground state.

to the T1 state results in a fast relaxation to the ground state. This process does not alter the main functioning of the VB2 defect but reduces its quantum efficiency.

Excitation to the second excited triplet T2 and single S2 states enables radiative decay. The corresponding energies and radiative decay rates are provided in Supplemental Table 4. Note that the absorption maximum of the T1 state (≈2.3 eV) is higher than the absorption maximum of the second excited triplet T2 (≈1.9 eV). Therefore, it is recommended to use below 2.3 eV excitation to avoid excitation to the T1 excited state and to retain the quantum efficiency of the defect.

The system can also decay non-radiatively from the T2 excited triplet state to the T1 excited triplet state, see Supplementary Figure 5. By using adiabatic and Franck-Condon approximations and an effective one phonon model[13–15], whose parameters can be found in Supplemental Table 5, we obtain $r_{\mathrm{NRD}} = 18.3$ MHz for the non-radiative decay rate at low temperature. By neglecting excitations to the dark T1 state and other non-spin conserving relaxation pathways, we obtain

Supplemental Table 5: Non-radiative decay rates as obtained from effective one phonon approximation. The table provides the generalized configuration coordinates differences (ΔQ), the total energy differences (ΔE), the phonon energies in the initial ($\hbar\omega_i$) and the final ($\hbar\omega_i$) states, the Huang-Rhys factor in the final state (S_f), and the electron-phonon coupling matrix elements (W_{if}) for the considered non-radiative transitions. From these parameters the rate of the spin conserving non-radiative decay (r_{NRD}) can be determined.

transition	ΔQ (amu$^{1/2}$ Å)	ΔE (meV)	$\hbar\omega_i$ (meV)	$\hbar\omega_f$ (meV)	S_f	W_{if} (eV/amu$^{1/2}$/Å)	r_{NRD} (MHz)
T2 $\rightarrow$ T1	1.24	603	89.7	93.9	17.2	3.15×10^{-4} *	18.3
T3 $\rightarrow$ T2	0.81271	292	103	106	8.39	6.91×10^{-3}	2.98×10^{4}

* The electron-phonon coupling matrix element $W_{if}(Q)$ is not constant over the path between the T2 and T1 excited state configurations due to the multiple single electron transitions involved in the non-radiative relaxation process. The W_{if} coupling constant is obtained by fitting. The standard error of the fitted value is 5.1×10^{-5} eV/amu$^{1/2}$/Å, the relative error is 16%.

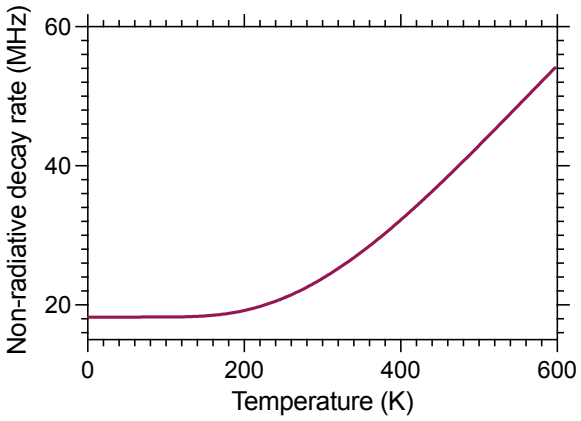

Supplemental Figure 6: Temperature dependence of the non-radiative decay rate between the T2 and T1 triplet excited states.

0.148 as an upper limit of the quantum efficiency of the VB2 defect, see Supplemental Table 4. The temperature dependence of the decay rate is depicted in Supplementary Figure 7 showing that the rate further increases beyond a threshold temperature of ≈200 K. The upper limit of the quantum efficiency is found to be 0.118 at 300 K.

The T3 excited state could in principle give rise to phonon emission, with 1.87 eV ZPL energy, however, the non-radiative decay from the T3 excited state to T2 excited state is highly efficient due to the relatively small, 291 meV energy difference of the states and the similarity of their atomic configurations ($\Delta Q = 0.81$). The corresponding non-radiative relaxation rate is as high as 29.8 GHz, which is four orders of magnitude larger than the radiative decay rate from the T3 excited state. Consequently, the quantum efficiency for the T3 excited state is 3.85×10^{-5}, see Supplemental Table 4. Due to the non-radiative decay, excitation to the T3 state dominantly results in a PL from the T2 excited state.

Thus, the dominant PL emission is obtained from the T2 and S2 excited states with ZPL energy 1.578 eV and 1.586 eV, respectively, that are ≈0.13 eV (or ≈60 nm) red-shifted compared to the ZPL transition energy of the V_B defect[16]. Note also that the triplet state is found to be ≈25% brighter than the singlet state. The calculated high-temperature phonon emission spectrum

Supplemental Table 6: Spin-orbit coupling matrix elements calculated on the level of NEVPT2.

		$\langle T\|LS\|S\rangle$, (GHz)		
singlet/triplet	configuration	$\|0\rangle$	$\|1\rangle$	$\|-1\rangle$
S0/T0	T0	0.02	0.00	0.00
S2/T2	T2	0.03	0.00	0.00
T2/S1	T2	2.10	0.00	0.00
S3/T3	T3	0.03	0.03	0.03
S2/T3	T3	0.00	16.31	16.31
S3/T2	T3	0.03	18.13	18.13

is depicted in Fig. 2b in the main text. By assuming 10% collection efficiency, the saturated intensity of the VB2 defect is in the order of 100 kcps. We note also that the quantum efficiency as well as the intensity of the PL signal are highly dependent on the excitation energy.

*** Inter-system crossing and spin non-conserving decay**

Besides spin-conserving optical and nonradiative decays, spin-dependent relaxation through inter-system crossings (ISCs) between the singlet and triplet manifolds is also possible. Such decay mechanisms are enabled by spin-orbit interaction and local vibrational modes. The spin-orbit coupling matrix elements calculated on the level of NEVPT2 are provided in Supplemental Table 6.

As we argued in the main text in connection with El-Sayed's rule, the coupling between the nearly degenerate singlet and triplet states is weak. This is confirmed by the calculations revealing small spin-orbit coupling between Sx and Tx excited state, where $x = \{0, 2, 3\}$, see Supplemental Table 6. Note that the obtained values are in the order of the numerical uncertainties of the applied method. Therefore, the values can be considered as upper limits for the spin-orbit coupling in this case. Using an effective one phonon model[13–15], we calculate the ISC decay rates for the most relevant spin non-conserving decay rates, see Supplemental Table 7. As can be seen, the decay

Supplemental Table 7: Inter-system crossing rates as obtained from effective one phonon approximation. The table provides the generalized configuration coordinates differences (ΔQ), the total energy differences (ΔE), the phonon energies in the initial ($\hbar\omega_i$) and the final ($\hbar\omega_i$) states, the Huang-Rhys factor in the final state (S_f), and the spin-orbit coupling matrix elements (λ) for the considered non-radiative transitions. From these parameters the rate of spin non-conserving decay (r_{ISC}) can be determined.

transition	ΔQ (amu$^{1/2}$ Å)	ΔE (meV)	$\hbar\omega_i$ (meV)	$\hbar\omega_f$ (meV)	S_f	λ (GHz)	r_{ISC} (MHz)
S0 $\rightarrow$ T0	9.60×10^{-3}	3.40	52.8	52.7	5.80×10^{-4}	0.018	2.53×10^{-5}
T2 $\rightarrow$ S2	0.175	12.2	93.7	93.7	0.343	0.030	3.32×10^{-5}
T2 $\rightarrow$ S1	1.24	603	89.7	93.9	17.2	2.10	9.71×10^{-4}
T3 $\rightarrow$ S2	0.813	292	103	106	8.39	18.1	0.561

rate from the S0 excited singlet state to the T0 ground state triplet state is $r_{\text{ISC}} = 25.3$ Hz at low temperature, which does not significantly change even at 300 K. We note also that the dipole-dipole coupling-induced spin relaxation of the S0 state is suppressed by the 3.3 meV exchange splitting of the S0 and T0 states. Consequently, the S0 excited state is long-lived and can serve as a memory to store population information.

Inter-system crossing between the different singlet-triplet branches can be more efficient. Indeed, we obtain $r_{\text{ISC}} = 0.561$ MHz ISC decay rate for the T3$\rightarrow$S3 transition. On the other hand, we obtain a small ISC rate for the T2$\rightarrow$S1 transition, $r_{\text{ISC}} = 0.971$ kHz, due to the small overlap of the phonon wavefunctions in the relaxed configurations of T1 and T2 excited states.

*** Single-shot read-out**

The T2 bright excited triplet state and the S0 bright excited singlet state have different lifetimes, thus the VB2 defect exhibits different PL intensities depending on the population of the singlet and triplet branches. Note also that the overall ISC rate between the triplet and singlet man-

ifolds under optical pumping that addresses only the T2 and S2 excited states is a few orders of magnitude smaller than the photon emission rate of the excited states. Consequently, the population of the singlet and triplet manifolds may be read out non-destructively before an ISC transition happens between them. Therefore, the time trace of the PL signal of a single VB2 defect exhibits jumps in the intensity that corresponds to quantum jumps between the singlet and the triplet manifolds as illustrated in Supplementary Figure 7. Due to the statistical noise of the photon collection, the quantum jumps are purely resolved even in optimal conditions, see Supplementary Figure 7. In order to read out the total spin state non-destructively with low statistical errors, the radiative lifetime of the excited state needs to be reduced by nanophotonic cavities[17].

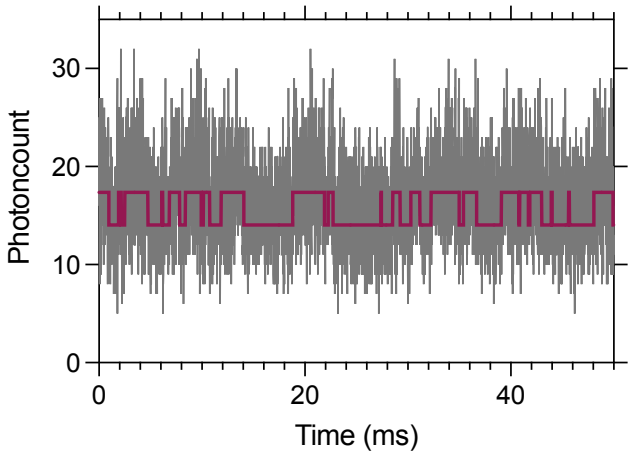

Supplemental Figure 7: Quantum jumps in the photoluminescence signal of the VB2 defect. In the calculation, we use 10 μs time bin and assume optimal conditions, i.e. 100% photon collection efficiency and saturated PL signal.

* Optical spin state initialization and optically detected magnetic resonance

As can be seen in Supplemental Table 6, the spin-orbit coupling matrix element between the low energy singlet-triplet pairs, S0/T0, S2/T2, and S1/T2, are strictly spin state selective, i.e. only transition to and from the $m_S = 0$ state in the triplet manifold is allowed. Therefore, any triplet-singlet-triplet double ISC transition polarizes the electron spin into the $|m_S = 0\rangle \equiv |0\rangle$ state.

Note also that the VB2 defect in the $|0\rangle$ and the $|\pm 1\rangle$ triplet spin states emits light with

different intensities. As no ISC is possible from $|\pm1\rangle$ spin state, the defect remains in the triplet state and emits with the corresponding PL intensity. On the other hand, ISC transitions are allowed for the $|0\rangle$ spin state, thus the time-averaged population is shared between the singlet state S0 and the $|0\rangle$ spin state of the T0 triplet ground state. Due to the lower PL intensity of the singlet manifold, the defect is dimmer when the spin is prepared in the $|0\rangle$ state, than $|\pm1\rangle$ state.

By applying a resonant microwave excitation between the split spin states in the triplet ground state the PL intensity of the VB2 defect changes. In such optically detected magnetic resonance (ODMR) measurement, the maximal continuous wave optical contrast of the different spin states is defined as

$$C_{\text{CW}}^{\text{max}} = \frac{I_{\text{MW-on}}}{I_{\text{MW-off}}} - 1 = \frac{I^{\pm} + I^{0}}{2I^{0}} - 1 \approx \frac{r_{\text{rad}}^{T0}\left(r_{\text{rad}}^{S0} + r_{\text{NRD}}\right)}{r_{\text{rad}}^{S0}\left(r_{\text{rad}}^{T0} + r_{\text{NRD}}\right) + r_{\text{rad}}^{T0}\left(r_{\text{rad}}^{S0} + r_{\text{NRD}}\right)} - \frac{1}{2} = +0.0459 \quad (1)$$

where $I^{\pm} = I^{\text{T0}}$, $I^{0} \approx \left(I^{\text{T0}} + I^{\text{S0}}\right)/2$, $I^{\text{T0}} = r_{\text{rad}}^{T0}/\left(r_{\text{rad}}^{T0} + r_{\text{NRD}}\right)$, and $I^{\text{S0}} = r_{\text{rad}}^{S0}/\left(r_{\text{rad}}^{S0} + r_{\text{NRD}}\right)$.

Note also that the ground state longitudinal spin relaxation has negative effects both on the spin state initialization and on the ODMR contrast. Due to the low ISC rate between the singlet and the triplet manifolds the dwell time in the ground state may be in the order of the spin relaxation time T1. To achieve maximal contrast, a high excitation rate is needed to shorten the dwell time in the ground state.

So far we have focussed on the spin polarization mechanism and the ODMR through the lowest five excited states, including only T2 and T1 triplets and S2, S1, and S0 singlets. It is apparent from the excited state energy spectrum, see Supplementary Figure 4, that the possible relaxation pathways considerably depend on the applied excitation energy. Higher than 1.86 eV excitation gives rise to additional, potentially more efficient ISCs between the third optically excited singlet-triplet states and the lower lying states, see Supplemental Table 6 and Supplemental Table 7. Therefore, higher energy excitation is preferable for spin state initialization. On the other hand, the increased probability of non-radiative decay and reduced quantum efficiency may quench the PL signal of the defect in such cases. A pulsed two-excitation laser setup can utilize the advantages of both the low and the high-energy excitations. For efficient spin state initialization one may use a strong 1.9-2.3 eV excitation laser, while for the read-out a strong, below 1.8 eV excitation

laser is recommended.

5 Supplementary Note 5 - Spin Hamiltonian of the VB2 defect

In this supplementary note, we discuss the peculiar features of the spin Hamiltonian of the VB2 defect that arise due to the defect's planar configuration and its unusual spin density. Throughout the discussion, we set the z axis parallel to the c-axis.

The total spin Hamiltonian of the defect including the most relevant interactions can be written as

$$H = H_{\text{ZFS}} + H_{\text{Zee}} + H_{\text{NucZee}} + H_{\text{hyperfine}} + H_{\text{Q}}, \tag{2}$$

where H_{ZFS} describes the zero-field splitting interaction,

$$H_{\text{Zee}} = g_e \mu_B \mathbf{SB} \tag{3}$$

describes the Zeeman interaction, where $g_e \approx 2$, μ_B is the Bohr magneton, $\mathbf{S}$ is the electron spin operator vector, and $\mathbf{B}$ is the magnetic field vector,

$$H_{\text{NucZee}} = -\mu_N \sum_i g_{N_i} \mathbf{I}_i \mathbf{B} \tag{4}$$

describes the nuclear Zeeman interaction, where μ_N is the nuclear magneton, g_{N_i} is the nuclear g-factor of nuclei i, and $\mathbf{I}_i$ is the nuclear spin operator vector of nuclei i, $H_{\text{hyperfine}}$ describes the hyperfine interaction, and H_{Q} describes the quadrupole interaction. Details on the zero-field interaction, the hyperfine interaction, and the quadrupole interaction are provided in the subsequent sections.

* Zero-field splitting

First of all, we note that the spin-orbit contribution to the zero-field splitting (ZFS) is marginal, found to be 11 MHz on the level NEVPT2, therefore we neglect it hereinafter. Due to symmetry reasons, the spin-spin zero-field splitting tensor takes the following form in our coordinate system with $z \parallel c$

$$D = \begin{pmatrix} D_{xx} & D_{xy} & 0 \\ D_{xy} & D_{yy} & 0 \\ 0 & 0 & D_{zz} \end{pmatrix}. \tag{5}$$

After diagonalization, the tensor can be written as

$$D = \begin{pmatrix} D_{x'} & 0 & 0 \\ 0 & D_{y'} & 0 \\ 0 & 0 & D_z \end{pmatrix}, \tag{6}$$

where $D_z = D_{zz}$ corresponds to an eigenvector parallel to the original z axis. $D_{x'}$ and $D_{y'}$ correspond to inplane eigenvector that defines the rotated x and y axes, x' and y' respectively.

The diagonal elements $D_{x'}$, $D_{y'}$, and D_z of the ZFS tensor obtained from spin contamination error corrected DFT calculations are 386.2 MHz, -929.2 MHz, and 542.6 MHz, respectively. Using higher level NEVPT2 theory but smaller model of the VB2 structure we obtain 632.9 MHz, -1383.2 MHz, and 750.3 MHz $D_{x'}$, $D_{y'}$, and D_z diagonalized ZFS tensor elements, respectively. The two methods qualitatively agree on the structure of the ZFS tensor, while we attribute the small numerical differences to the quantum confinement effects. Hereinafter we use the DFT ZFS results.

According to the convention, the quantization direction is defined by the eigenvector of the largest absolute diagonal element. In the case of the VB2 defect, the conventional quantization direction is y' corresponding to the diagonal element D'_y. The obtained ZFS parameters are $D = 1.394$ GHz and $E = 78.2$ MHz. Here, we note that a similar D value has been recently reported in neutron irradiated hBN samples in Refs. [18,19]

Note on the other hand that there is an inconsistency between the quantization axes defined by the ZFS and the spin-orbit interaction in the ISC processes. As we have seen before, the spin selectivity is defined in the quantization basis parallel to the c axis, while using the ZFS tensor the conventional quantization axis is in-plane. Such an inconsistency is only possible for low symmetry defect configurations, like the VB2 defect. Throughout this study, we use the polarization basis defined by the spin-orbit interaction as our quantization basis. The corresponding non-conventional ZFS parameter are $\widetilde{D} = -814$ MHz and $\widetilde{E} = -658$ MHz.

The ZFS spin Hamiltonian can be written as

$$\hat{H}_{\text{ZFS}} = \mathbf{S}D\mathbf{S} = D_{x'}S_{x'}^2 + D_{y'}S_{y'}^2 + D_zS_z^2. \tag{7}$$

In the polarization basis, the matrix form of the Hamiltonian reads as

$$H_{ZFS} = \frac{1}{2}\begin{pmatrix} D_z & 0 & D_{x'} - D_{y'} \\ 0 & -2D_z & 0 \\ D_{x'} - D_{y'} & 0 & D_z \end{pmatrix}, \tag{8}$$

The $|0\rangle$ state, in which the system is polarized in the optical cycle, is a good eigenstate of the Hamiltonian, while the $|\pm 1\rangle$ states mix and form new eigenstates of the zero magnetic field Hamiltonian, $|+\rangle = (|-1\rangle + |+1\rangle)/\sqrt{2}$ and $|-\rangle = (|-1\rangle - |+1\rangle)/\sqrt{2}$. After diagonalization of the ZFS spin Hamiltonian matrix, we obtain the following eigenvalues of -929.2, 386.2, and 542.6 MHz for the eigenstates $|+\rangle$, $|-\rangle$, and $|0\rangle$ that correspond to the D'_y, D'_z, and D_z ZFS diagonal matrix elements, respectively. The observed level structure exhibits a giant effective transverse ZFS splitting $2\widetilde{E} = 1.315$ GHz.

*** Hyperfine and quadrupole interaction**

The hyperfine Hamiltonian term can be written as

$$H_{\text{hyperfine}} = \sum_i \mathbf{S} A_i \mathbf{I}_i, \tag{9}$$

where A_i is the hyperfine tensor and $\mathbf{I}_i$ is the nuclear spin operator vector of nuclei i. As the most abundant boron and nitrogen nuclei posses total spin $I > 1$, quadrupole interaction needs to be taken into account as well. The corresponding Hamiltonian term can be written as

$$H_Q = \frac{C_q}{4I\,(2I-1)} \sum_i I_{z,i}^2, \tag{10}$$

where parameter C_q defines the coupling strength.

We provide the sites of strong hyperfine interactions and the corresponding hyperfine tensors in Supplementary Figure 8 and in Supplemental Table 8, respectively. The values in the table are obtained considering ^{11}B and ^{14}N isotopes, whose natural abundances are 80.1% and 99.5%, respectively. Due to symmetry reasons the A_{xz} and A_{yz} elements of the tensor are zero, therefore the hyperfine splitting is $A_z = A_{zz}$.

Table 9 provides the calculated quadrupole parameters for the neighboring sites of the neutral unstrained VB2 defect as well as for the perfect hBN structure. As can be seen, there are several

Supplemental Table 8: Relevant hyperfine coupling tensors for the most abundant boron and nitrogen nuclei in the triplet ground state of the VB2 defect in non-strained and +5% strained configurations. For the considered sites see Supplementary Figure 8. Due to symmetry constraints the A_{xz} and the A_{yz} element of the tensor are zero. Our coordinate system is chosen so that the y-axis is parallel to the axis of the double vacancy sites of the VB2 configuration and the z-axis is perpendicular to the BN plane. All values are in MHz.

strain	no strain				+5% strain			
position	A_{xx}	A_{yy}	A_{zz}	A_{xy}	A_{xx}	A_{yy}	A_{zz}	A_{xy}
N_1	5.194	5.582	60.483	-0.037	3.621	4.261	63.535	0.322
N_2	83.332	55.465	50.377	16.522	63.070	31.294	18.682	26.859
N_3	65.008	48.842	45.621	-9.772	10.190	7.503	6.847	-1.726
N_{1l}	-0.794	-0.826	10.197	-0.183	0.170	0.723	9.217	-0.216
B_{2l}	-6.780	-1.138	-8.663	-0.495	-13.168	-6.787	-15.538	-2.169
B_{2r}	2.224	4.083	-2.872	-4.344	-14.982	-12.293	-19.693	-4.295
B_{3r}	-4.623	-1.849	-6.359	-0.284	-0.610	-0.605	-1.593	-0.416

Supplemental Table 9: Relevant quadrupolar parameters C_q of the neighbouring atoms of the VB2 defect. For comparison, we also provide C_q parameters for the perfect hBN structure. All values are in MHz and provided for the most abundant boron and nitrogen nuclei.

VB2	
position	C_q
B	-5.622
N_1	4.276
N_2	1.889
N_3	-0.787
N_{1l}	3.971
perfect	
position	C_q
B	3.717
N	0.022

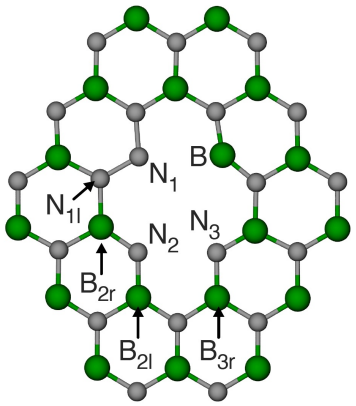

Supplemental Figure 8: Nuclear spin sites of strong hyperfine coupling.

quadrupole parameters that deviate from the bulk values. In particular, the closest nitrogen atoms exhibit sizeable quadrupole splitting in the VB2 configuration.

*** Notes on the spin properties**

Due to symmetry and the low dimensionality of the structure, the hyperfine Hamiltonian specified in Eq. (9) includes terms that neither account for nuclear spin precession nor electron spin precession. The only non-vanishing hyperfine terms can be described by the $S_z I_z$ and the $S_\pm I_\mp$ and $S_\pm I_\pm$ operator combinations that account for hyperfine splitting and mutual flip-flops of the electron and nuclear spins. The hyperfine splitting is zero for the $|0\rangle$ electron spin state as well as for the $|\pm\rangle$ mixed spin states due to the transverse zero-field splitting governed by $\widetilde{E}$. It is important to note that the spin flip-flop terms are largely suppressed by the splitting of the electron spin states that are typically an order of magnitude larger than the hyperfine interaction. Consequently, the hyperfine splitting is vanishing at $B = 0$. The residual splitting is due to the weak mixing of the electron spin states $|0\rangle$ and $|\pm\rangle$ induced by the spin flip-flop terms. The spin mixing is the strongest between the $|0\rangle$ and $|-\rangle$ pair of states whose splitting is the smallest.

Magnetic field dependence of the hyperfine structure is depicted in Supplementary Figure 9. As can be seen, the $\widetilde{E}$ splitting that appears for the perpendicular to plane quantization axis suppresses the hyperfine splitting of the lower branch, that corresponds to the state $|+\rangle$, at $B = 0$.

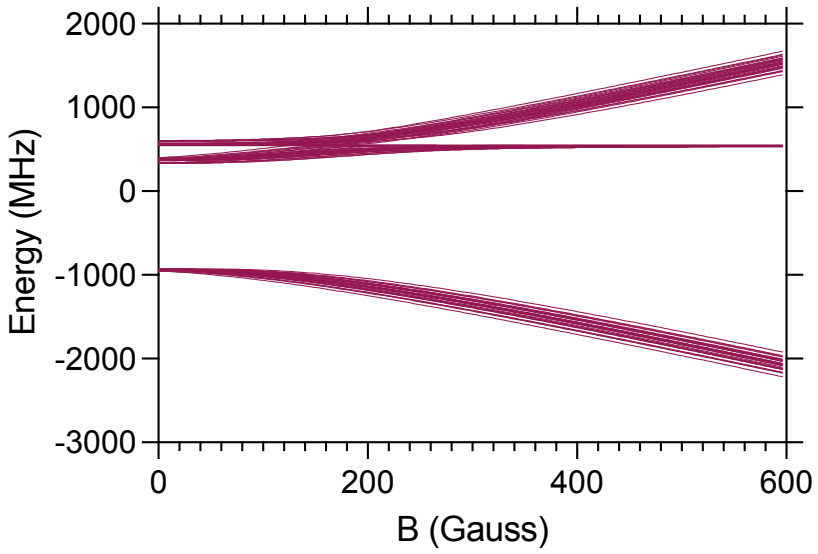

Supplemental Figure 9: Fine and hyperfine energy level structure of the VB2 center interacting with its first nearest neighbour ^{14}N nitrogen nuclei. The magnetic field is set parallel to the c axis.

The suppression of the hyperfine interaction has a favorable effect on the spin coherence and the ODMR linewidth, see main text. Due to the dense nuclear spin bath of the host material, such decoherence protection schemes may be of crucial importance for practical qubit applications in hBN.

Recent developments in understanding C_{1h} symmetric divacancy qubits in SiC have revealed related decoherence protection scheme[20] that utilizes the E splitting and resonant driving between the $|\pm\rangle$ states. The larger the E splitting, the more efficient the suppression of magnetic $1/f$ noise. Here, we note that the value of the transverse zero-field splitting depends on the quantization axis, while the spin properties and the dynamics do not. An alternative interpenetration of the spin properties of the VB2 defect can be obtained by using the conventional in-plane quantization axis obtained as the principal axis of the diagonalized ZFS tensor. In this basis, the lower lying state is the $|0\rangle$ while the highest one is the $|+\rangle$ state at zero magnetic fields.

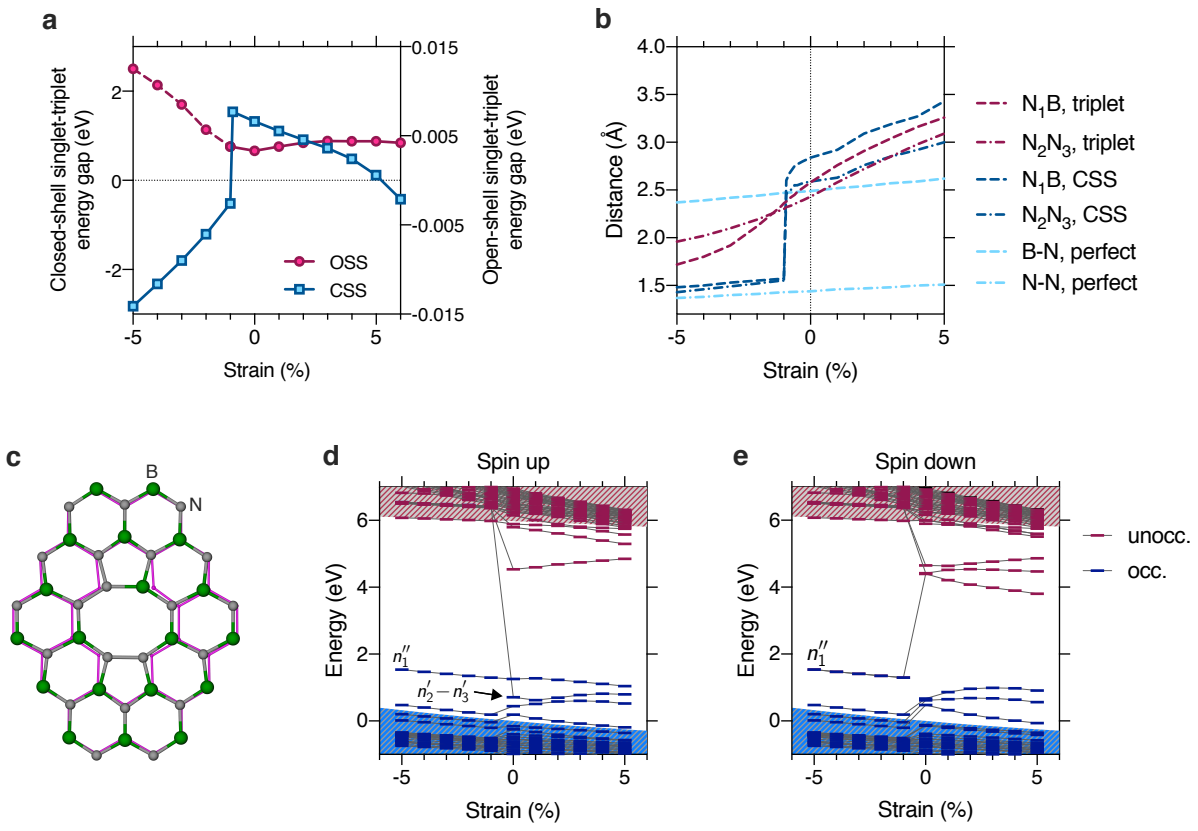

Supplemental Figure 10: Strain dependence of the electronic structure of the VB2 defect. **a** Biaxial strain dependence of the open-shell singlet (OSS)-triplet (blue) and the closed-shell singlet (CSS)-triplet (red) splitting. The triplet state is stable in the $\{-0.9\%, +5.0\%\}$ strain interval. The sudden change observed at -0.9% strain is due to the creation of new bonds. **b** Strain dependence of atomic distances in the triplet (red) and the CSS (dark blue) states of the VB2 defect as well as in the perfect hBN lattice (light blue). **c** Structure of the CSS ground state (green and grey balls) and the triplet state (pink wire frame) at -1% strain. **d** and **e** Strain dependence of the Kohn-Sham electronic structure as obtained from HSE(0.32) calculations for the spin-up and spin-down channels, respectively.

6 Supplementary Note 6 - Strain dependence of the electronic structure

Strain is an important factor in exfoliated few-layer materials[21,22], that in turn makes the control of single photon emitters' and qubits' electronic structure possible[23–26]. Since the VB2 configuration

is a vacancy complex with bonding and anti-bonding planar defect orbitals, the electronic structure may be highly sensitive to applied strain. In Supplementary Figure 10a, we study the dependence of the open-shell singlet (OSS)-triplet and the closed-shell singlet (CSS)-triplet gaps on the applied biaxial strain. As can be seen, the triplet state is always slightly more favorable than the OSS state. By stretching the structure the 3.3 meV gap observed at zero strain increases to 5 meV. This is due to the fact that the n_2' and n_3' dangling bonds no longer form bonding and anti-bonding states in the stretched configurations and the spin density is only formed by n_1'' and n_2' states, in contrast to the unstrained case. The change in the localization gives rise to a slight increase in the exchange energy. By further stretching the structure, the CSS state became energetically favorable.

For negative strain, we observe a sudden change in the CSS-triplet energy splitting, i.e. for strain greater than -0.9% the CSS state becomes the ground state after the creation of new bonds and rearrangement of the electronic structure. In Supplementary Figure 10b we plot the distances of the N_1 and B and the N_2 and N_3 atoms in the triplet and in the CSS configuration as a function of the applied biaxial stain. For the sake of comparison, we also show the nearest neighbor nitrogen-boron bond length and the second nearest neighbor nitrogen-nitrogen distance in the defect-free strained hBN structure. As can be seen, the atomic distances continuously change in the triplet state. Notably, the distances of the neighboring atoms of the double vacancy change considerably faster than the atomic distances in the perfect hBN structure. This indicates that the VB2 complex absorbs the stress applied to the defective hBN structure. For the CSS electronic configuration, we observe a jump in the atomic distances at -0.9% strain, where both the N_1 and B and the N_2 and N_3 distances change from the level of second nearest neighbor distance to first neighbor distance, see Supplementary Figure 10b. The formation of a pair of new bonds and two pentagons is clearly visible in Supplementary Figure 10c. Considering the Kohn-Sham electronic structure as obtained by HSE(0.32) functional, we observe drastic changes at -0.9% strain, see Supplementary Figure 10d and e. In the triplet ground state the anti-bonding $n_2' - n_3'$ and the n_1'' orbitals are half occupied. When the new bonds are formed, the electron from the anti-bonding state is moved to the n_1'' orbital to give rise to a closed shell configuration. In addition, the fully occupied n_1' and the unoccupied b' states mix and form a fully occupied $n_1' + b'$ bonding state and an unoccupied

$n_1' - b'$ anti-bonding state. The former state appears in the valence band, while the latter appears in the conduction band.

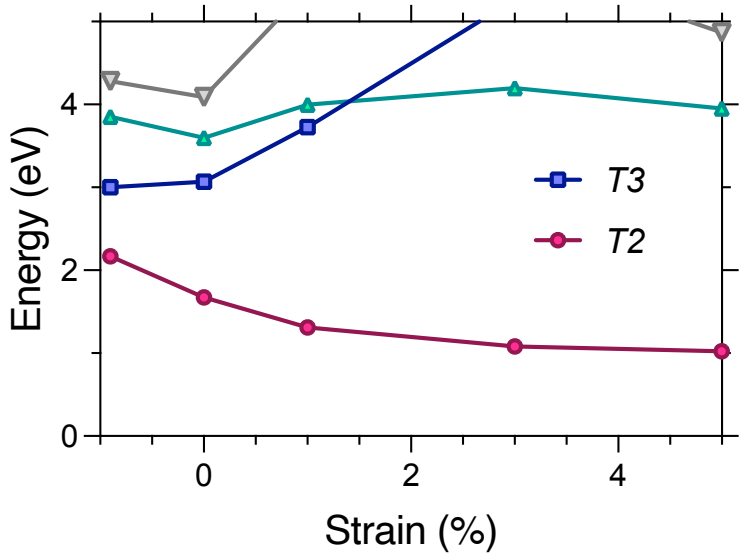

Supplemental Figure 11: Uni-axial strain dependence of the vertical excited state energy spectrum obtained by DMRG calculations using HSE(0.32) relaxed ground state atomic configurations. The figure depicts only the triplet energy states.

Variation of the many-body energy level structure as a function of the applied uni-axial strain is investigated on the level of DMRG, see Supplementary Figure 11. As can be seen, the energy of the second excited triplet state T2 monotonously decreases, while the energy of the third excited triplet state T3 monotonously increases as the structure is stretched. This is in-line with the observed transitions in the single particle energy structure showing the decomposition of the $n_2' \pm n_3'$ bonding and anti-bonding orbitals in the stretched configuration. These results indicate that the ZPL energy of the VB2 center decreases with applied strain. Strain dependence of the optical signal of the VB2 center can be used to monitor the local strain in the hBN sample.

Strain dependence of the conventional and the non-conventional ZFS parameters is depicted in Supplementary Figure 12 for the $\{-0.9\%, +5.0\%\}$ strain interval. As can be seen, the ZFS parameters depend only slightly on the applied strain as large as $+5\%$. More specifically, positive

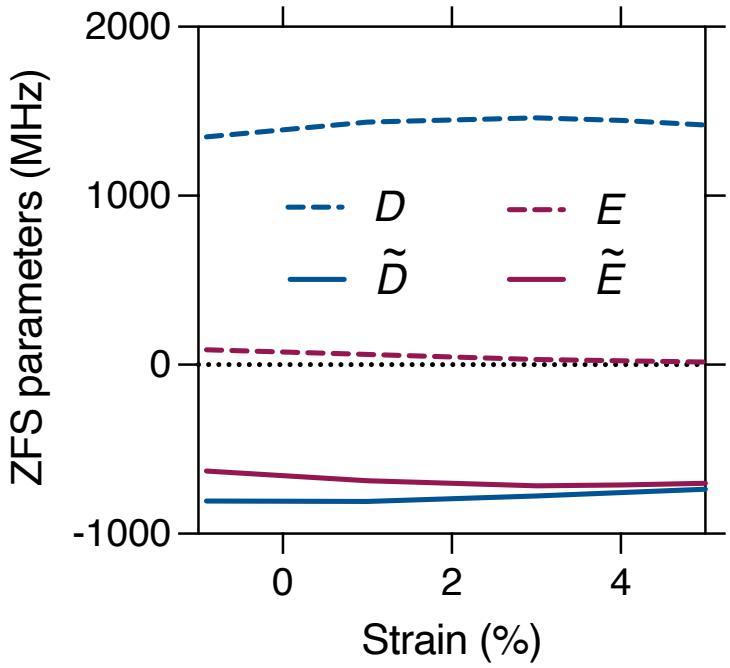

Supplemental Figure 12: Uni-axial strain dependence of the conventional ZFS parameters (D and E) and the non-conventional ZFS parameter ($\widetilde{D}$ and $\widetilde{E}$), which are defined by using a perpendicular to plane quantization axis.

strain tends to reduce the transverse ZFS splitting in the conventional basis whose quantization axis is nearly parallel to the V_B-V_N axis. Accordingly, the non-conventional ZFS parameters, defined in the polarization basis, approach degeneracy.

Strain dependence of the hyperfine tensors is investigated in Supplemental Table 8, where we provide the hyperfine values for the unstrained configuration and for the +5% uniaxially strained configuration. Note that for the 5% stretched configuration the spin density redistributes and localizes dominantly on N_1 and N_2 nitrogen atoms. The hyperfine tensors listed in Supplemental Supplemental Table 8 change accordingly, i.e. the hyperfine values marginally change for the N_1 site, slightly reduce for the N_2 site, and considerably reduce for the N_3 site. It is notable, however, that the hyperfine interaction considerably increases on the first neighbor borons, B_{2l} and B_{2r}, of the N_2 sites.

References

1. Heyd, J., Scuseria, G. E. & Ernzerhof, M. Hybrid functionals based on a screened coulomb potential. *J. Chem. Phys.* **118**, 8207 (2003). URL http://dx.doi.org/10.1063/1.1564060.

2. Heyd, J., Scuseria, G. E. & Ernzerhof, M. Erratum: "hybrid functionals based on a screened coulomb potential" [j. chem. phys. 118, 8207 (2003)]. *J. Chem. Phys.* **124**, 219906 (2006). URL http://dx.doi.org/10.1063/1.2204597.

3. Weston, L., Wickramaratne, D., Mackoit, M., Alkauskas, A. & Van de Walle, C. G. Native point defects and impurities in hexagonal boron nitride. *Phys. Rev. B* **97**, 214104 (2018). URL https://link.aps.org/doi/10.1103/PhysRevB.97.214104.

4. Strand, J., Larcher, L. & Shluger, A. L. Properties of intrinsic point defects and dimers in hexagonal boron nitride. *Journal of Physics: Condensed Matter* **32**, 055706 (2019). URL https://doi.org/10.1088/1361-648x/ab4e5d.

5. Toledo, J. R. *et al.* Electron paramagnetic resonance signature of point defects in neutron-irradiated hexagonal boron nitride. *Phys. Rev. B* **98**, 155203 (2018). URL https://link.aps.org/doi/10.1103/PhysRevB.98.155203.

6. Gottscholl, A. *et al.* Initialization and read-out of intrinsic spin defects in a van der Waals crystal at room temperature. *Nature Materials* **19**, 540–545 (2020). URL https://www.nature.com/articles/s41563-020-0619-6. Number: 5 Publisher: Nature Publishing Group.

7. Fischer, M. *et al.* Controlled generation of luminescent centers in hexagonal boron nitride by irradiation engineering. *Science Advances* **7**, eabe7138 (2021). URL https://advances.sciencemag.org/content/7/8/eabe7138. Publisher: American Association for the Advancement of Science Section: Research Article.

8. Kianinia, M., White, S., Fröch, J. E., Bradac, C. & Aharonovich, I. Generation of Spin Defects in Hexagonal Boron Nitride. *ACS Photonics* **7**, 2147–2152 (2020).

URL https://doi.org/10.1021/acsphotonics.0c00614. Publisher: American Chemical Society.

9. Ghaderzadeh, S., Kretschmer, S., Ghorbani-Asl, M., Hlawacek, G. & Krasheninnikov, A. V. Atomistic Simulations of Defect Production in Monolayer and Bulk Hexagonal Boron Nitride under Low- and High-Fluence Ion Irradiation. *Nanomaterials* **11**, 1214 (2021). URL https://www.mdpi.com/2079-4991/11/5/1214. Number: 5 Publisher: Multidisciplinary Digital Publishing Institute.

10. Gao, X. *et al.* Femtosecond Laser Writing of Spin Defects in Hexagonal Boron Nitride. *ACS Photonics* **8**, 994–1000 (2021). URL https://doi.org/10.1021/acsphotonics.0c01847. Publisher: American Chemical Society.

11. Chen, Y. & Quek, S. Y. Photophysical Characteristics of Boron Vacancy-Derived Defect Centers in Hexagonal Boron Nitride. *The Journal of Physical Chemistry C* **125**, 21791–21802 (2021). URL https://doi.org/10.1021/acs.jpcc.1c07729. Publisher: American Chemical Society.

12. Gali, A., Janzén, E., Deák, P., Kresse, G. & Kaxiras, E. Theory of spin-conserving excitation of the n-v^- center in diamond. *Phys. Rev. Lett.* **103**, 186404 (2009).

13. Alkauskas, A., Yan, Q. & Van de Walle, C. G. First-principles theory of nonradiative carrier capture via multiphonon emission. *Physical Review B* **90**, 075202 (2014). URL https://link.aps.org/doi/10.1103/PhysRevB.90.075202.

14. Wu, F., Smart, T. J., Xu, J. & Ping, Y. Carrier recombination mechanism at defects in wide band gap two-dimensional materials from first principles. *Physical Review B* **100**, 081407 (2019). URL https://link.aps.org/doi/10.1103/PhysRevB.100.081407. Publisher: American Physical Society.

15. Turiansky, M. E. *et al.* Nonrad: Computing nonradiative capture coefficients from first principles. *Comput. Phys. Commun.* **267**, 108056 (2021).

16. Ivády, V. *et al.* Ab initio theory of the negatively charged boron vacancy qubit in hexagonal boron nitride. *npj Computational Materials* **6**, 1–6 (2020). URL https://www.nature.com/articles/s41524-020-0305-x. Number: 1 Publisher: Nature Publishing Group.

17. Fröch, J. E. *et al.* Purcell Enhancement of a Cavity-Coupled Emitter in Hexagonal Boron Nitride. *Small* **18**, 2104805 (2022). URL https://onlinelibrary.wiley.com/doi/abs/10.1002/smll.202104805. _eprint: https://onlinelibrary.wiley.com/doi/pdf/10.1002/smll.202104805.

18. Toledo, J. R. *et al.* Electron paramagnetic resonance signature of point defects in neutron-irradiated hexagonal boron nitride. *Physical Review B* **98**, 155203 (2018). URL https://link.aps.org/doi/10.1103/PhysRevB.98.155203. Publisher: American Physical Society.

19. Huseynov, E. M. *et al.* EPR spectroscopy of neutron irradiated nanocrystalline boron nitride (h-BN) particles. *Ceramics International* **47**, 7218–7223 (2021). URL https://www.sciencedirect.com/science/article/pii/S0272884220333915.

20. Miao, K. C. *et al.* Universal coherence protection in a solid-state spin qubit. *Science* **369**, 1493–1497 (2020). URL https://science.sciencemag.org/content/369/6510/1493.

21. Lloyd, D. *et al.* Band Gap Engineering with Ultralarge Biaxial Strains in Suspended Monolayer MoS2. *Nano Letters* **16**, 5836–5841 (2016). URL https://doi.org/10.1021/acs.nanolett.6b02615. Publisher: American Chemical Society.

22. Peng, Z., Chen, X., Fan, Y., Srolovitz, D. J. & Lei, D. Strain engineering of 2D semiconductors and graphene: from strain fields to band-structure tuning and photonic applications. *Light: Science & Applications* **9**, 190 (2020). URL

https://www.nature.com/articles/s41377-020-00421-5. Number: 1 Publisher: Nature Publishing Group.

23. Grosso, G. *et al.* Tunable and high-purity room temperature single-photon emission from atomic defects in hexagonal boron nitride. *Nature Communications* **8**, 705 (2017). URL https://www.nature.com/articles/s41467-017-00810-2. Number: 1 Publisher: Nature Publishing Group.

24. Proscia, N. V. *et al.* Near-deterministic activation of room-temperature quantum emitters in hexagonal boron nitride. *Optica* **5**, 1128–1134 (2018). URL https://www.osapublishing.org/optica/abstract.cfm?uri=optica-5-9-1128. Publisher: Optical Society of America.

25. Yim, D., Yu, M., Noh, G., Lee, J. & Seo, H. Polarization and Localization of Single-Photon Emitters in Hexagonal Boron Nitride Wrinkles. *ACS Applied Materials & Interfaces* **12**, 36362–36369 (2020). URL https://doi.org/10.1021/acsami.0c09740. Publisher: American Chemical Society.

26. Mendelson, N., Doherty, M., Toth, M., Aharonovich, I. & Tran, T. T. Strain-Induced Modification of the Optical Characteristics of Quantum Emitters in Hexagonal Boron Nitride. *Advanced Materials* **32**, 1908316 (2020). URL https://onlinelibrary.wiley.com/doi/abs/10.1002/adma.201908316. _eprint: https://onlinelibrary.wiley.com/doi/pdf/10.1002/adma.201908316.